



# Machine learning-enabled on-mask triboelectric textile electronic system for real-time respiratory dynamics monitoring

Jia Zhao<sup>1,2,#</sup>, Xiaosen Pan<sup>1,2,#</sup> , Ming Yuan<sup>1,2</sup>, Yunxiang Long<sup>1,2,3</sup>, Yi Niu<sup>1,2</sup>, Yuyang Sun<sup>1,2,4</sup>, Jun Wang<sup>5</sup>, Ting Lin<sup>4</sup>, Junjie Gan<sup>6</sup>, Feng Xu<sup>1,2,\*</sup> , Yunsheng Fang<sup>1,2,\*</sup> 

## Keywords:

Triboelectric sensors, textile electronics, plasma treatment, respiratory monitoring, machine learning

## Citation:

Zhao, J.; Pan, X.; Yuan, M.; Long, Y.; Niu, Y.; Sun, Y.; Wang, J.; Lin, T.; Gan, J.; Xu, F.; Fang, Y. Machine learning-enabled on-mask triboelectric textile electronic system for real-time respiratory dynamics monitoring. *Soft Sci.* 2026, 6, 4. <https://dx.doi.org/10.20517/ss.2025.93>

Received: 22 Sep 2025

First Decision: 14 Oct 2025

Revised: 4 Nov 2025

Accepted: 19 Nov 2025

Published: 16 Jan 2026

## Academic Editor:

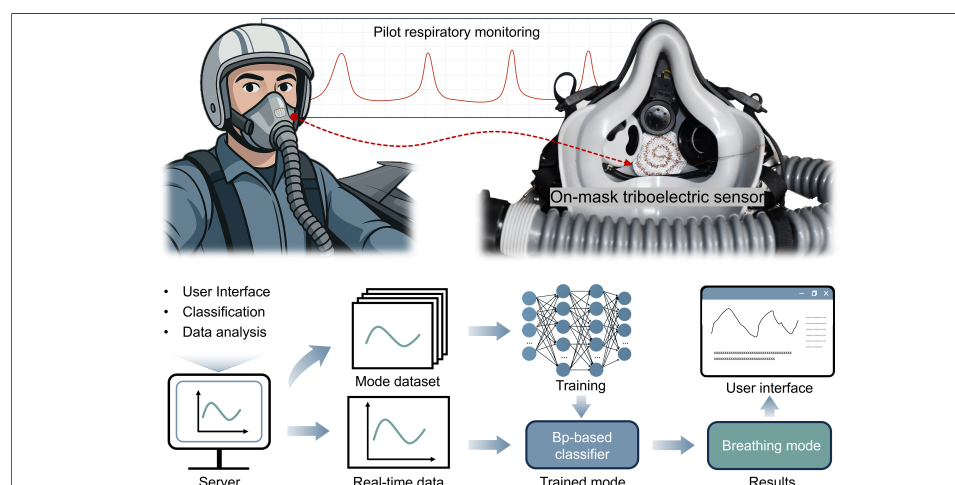
Carlo Massaroni

## Copy Editor:

Xing-Yue Zhang

## Production Editor:

Xing-Yue Zhang



## Abstract

Real-time and accurate respiratory monitoring is crucial in extreme conditions, such as high-altitude aviation, critical care, and hazardous occupations, where subtle respiratory changes may rapidly escalate into life-threatening events. However, existing respiratory support systems are often cumbersome, insensitive to nuanced breathing patterns, or susceptible to environmental interference. Herein, we introduce a highly sensitive, plasma-modified triboelectric textile sensor integrated into an oxygen mask for real-time respiratory dynamics monitoring. By engineering nanoscale surface roughness and surface modification via plasma treatment, the sensor achieves a remarkable 420% enhancement in output voltage, yielding high sensitivity ( $2.02 \text{ V} \cdot \text{kPa}^{-1}$ ), rapid response (96 ms), and excellent stability (over 95% signal retention after 90 days). Integrated with a machine learning-assisted classifier, the system achieves 97.2% accuracy in respiratory pattern recognition, while automatically discriminating authentic breathing signals from artifacts.

<sup>1</sup>The Key Laboratory of Biomedical Information Engineering of the Ministry of Education, School of Life Science and Technology, Xi'an Jiaotong University, Xi'an 710049, Shaanxi, China.

<sup>2</sup>Bioinspired Engineering & Biomechanics Center (BEBC), Xi'an Jiaotong University, Xi'an 710049, Shaanxi, China.

<sup>3</sup>Department of Hepatobiliary Surgery and Liver Transplantation, The Second Affiliated Hospital of Xi'an Jiaotong University, Xi'an 710004, Shaanxi, China.

<sup>4</sup>Department of Surgical Intensive Care Units, The First Affiliated Hospital of Xi'an Jiaotong University, Xi'an 710061, Shaanxi, China.

<sup>5</sup>Department of Health Evaluation and Promotion, The First Affiliated Hospital of Xi'an Jiaotong University, Xi'an 710061, Shaanxi, China.

<sup>6</sup>Avic Aerospace Life-Support Industries, LTD., Xiangyang 430030, Shaanxi, China.

#Authors contributed equally.

\*Correspondence to: Prof. Feng Xu, Prof. Yunsheng Fang, The Key Laboratory of Biomedical Information Engineering of the Ministry of Education, School of Life Science and Technology, Xi'an Jiaotong University, Xi'an 710049, Shaanxi, China. E-mail: fengxu@mail.xjtu.edu.cn; ysfang@xjtu.edu.cn

With a customized electronic circuit and an application terminal, the on-mask intelligent system provides immediate feedback for adaptive oxygen regulation. This capability is of paramount importance for improving oxygen-management efficiency and safeguarding the lives of personnel operating under extreme conditions.

## INTRODUCTION

Respiratory rhythm serves as a critical physiological barometer for homeostatic regulation to internal and external perturbations<sup>[1,2]</sup>. In extreme settings such as high altitude, deep sea, and industrial environments, variations in ambient pressure, gas composition, or individual physiological constraints induce significant fluctuations in breathing rate, ventilation volume, and rhythm, which in severe cases may affect life safety<sup>[3]</sup>. Real-time monitoring coupled with external oxygen supplementation is therefore essential to maintain vital signs such as arterial oxygen saturation. Fighter pilots represent the most stringent example of this requirement during maneuvers, generating extremely high G-forces<sup>[4]</sup>. Oxygen delivery must precisely match instantaneous metabolic demand to prevent gravity-induced loss of consciousness from insufficient oxygen partial pressure or pulmonary and central nervous system toxicity arising from over-oxygenation<sup>[5]</sup>. Thus, it is imperative to develop a highly sensitive sensor system capable of capturing and identifying respiratory dynamics in real-time, while issuing early warnings upon detection of abnormal patterns<sup>[6-8]</sup>.

Wearable respiratory sensing technology has emerged as a continuous, noninvasive approach for monitoring respiratory dynamics<sup>[9-13]</sup>. Currently, strain sensors with inherent sensitivity and form-factor constraints have been deployed, which also necessitate tight adhesion or binding to the abdominal<sup>[14-16]</sup>, thoracic<sup>[17,18]</sup>, cervical<sup>[19]</sup>, or facial skin<sup>[20,21]</sup>. During multiaxial acceleration in fighter operations, contact-based monitoring often suffers from signal drift, classification errors, and discomfort from unstable contact<sup>[22,23]</sup>. Thus, non-contact approaches such as humidity sensors that measure exhaled moisture are employed to monitor respiratory rhythm<sup>[24-29]</sup>. However, slow response and recovery rates, along with signal degradation caused by moisture accumulation, make these devices unsuitable for real-time, high-precision monitoring in extreme environments<sup>[30,31]</sup>. In contrast, triboelectric sensors offer high sensitivity, lightweight structure, and excellent robustness, enabling accurate capture of respiratory airflow variations under non-contact conditions<sup>[32-37]</sup>. Inevitably, excessive sensitivity also amplifies environmental vibrations and motion artifacts<sup>[38]</sup>. Moreover, these respiratory monitoring paradigms mostly focus on sensor design without considering the electronic circuit hardware support and precise algorithm development, thus making it difficult for them to truly adapt to extreme operational settings. Therefore, the integration of tailored signal-processing algorithms with hardware systems is required to suppress interference, extract key respiratory features, and provide real-time feedback<sup>[39]</sup>.

In this context, we propose a machine learning-enhanced on-mask respiratory electronic system integrated with a proprietary algorithm and application terminal, enabling real-time, continuous, and accurate respiratory dynamics monitoring. Specifically, low-pressure plasma treatment creates nanoscale roughness and surface modification on the triboelectric fibers, increasing their contact area and boosting output voltage by 420%. The optimized sensor exhibits a 96 ms response time and  $2.02 \text{ V} \cdot \text{kPa}^{-1}$  sensitivity. Moreover, the sensor maintains signal stability for 5,000 consecutive excitation cycles, and the output amplitude remains above 95% after 90 days of exposure. Leveraging machine-learning algorithms, the system classifies respiratory patterns with 97.2% accuracy while intelligently filtering pseudo-respiration artifacts and providing real-time warnings.



## EXPERIMENTAL

### Fabrication of the triboelectric fibers

Copper wires with a diameter of 200  $\mu\text{m}$  (99.95% purity) served as the conductive core for both triboelectric materials. For epoxy-coated fibers, the copper wires were uniformly coated with epoxy resin at a controlled withdrawal speed of 2 mm/s, and then dried using a hot plate with a temperature of 380  $^{\circ}\text{C}$ . For polyvinylidene fluoride (PVDF)-coated fibers, poly (vinylidene fluoride-co-hexafluoropropylene) (PVDF-HFP) was dissolved in N, N-dimethylformamide (DMF) at a weight concentration of 25% under magnetic stirring at 60  $^{\circ}\text{C}$  for 12 h. The copper wires were then dip-coated with the PVDF solution at the same withdrawal speed and dried at 380  $^{\circ}\text{C}$  to ensure complete solvent evaporation.

### Low-pressure plasma surface treatment

Low-pressure plasma treatment was performed using a radio-frequency plasma system (PTL-VM500, PTL Plasma, Shandong, China) operated at 13.56 MHz. The textile samples were placed in the plasma chamber and evacuated to achieve a vacuum level of 30–50 Pa. A gas mixture of argon and oxygen (1:1 ratio) was introduced at a controlled flow rate of 6  $\text{mL}\cdot\text{min}^{-1}$  to maintain the desired working pressure. The plasma power was set to 300 W, and treatment duration was varied from 15 to 75 min to optimize sensor performance. All plasma treatments were conducted at room temperature.

### Fabrication of the on-mask sensor

The coated wires were helically twisted together using a custom twisting apparatus to form flexible yarns and subsequently woven into textile structures using a plain weave pattern. The final textile was tailored into a circular shape with a diameter of 35 mm to fit within the airflow channel of standard pilot oxygen masks.

### Surface morphology characterization

Surface morphology of the triboelectric fibers was characterized using a scanning electron microscope (ZEISS SIGMA 360, Carl Zeiss AG, Oberkochen, Germany). Energy dispersive spectroscopy (EDS) mapping was performed using the same scanning electron microscopy (SEM) system to analyze elemental composition changes after plasma treatment. Chemical modifications induced by plasma treatment were analyzed using Fourier Transform Infrared (FTIR) spectroscopy (PerkinElmer Spectrum 3, PerkinElmer, Waltham, MA, USA) and X-ray photoelectron spectroscopy (XPS; PHI GENESIS 500, ULVAC Inc., Kanagawa, Japan). Spectra were recorded from 4,000 to 500  $\text{cm}^{-1}$ . Three-dimensional surface topography was measured using atomic force microscopy (SPM-9700HT, Shimadzu Corporation, Kyoto, Japan). Scan areas of 5  $\mu\text{m} \times 5 \mu\text{m}$  were analyzed for each sample, and surface roughness parameters, including arithmetic mean roughness ( $R_a$ ) and root mean square roughness ( $R_q$ ), were calculated using SPM-9700 Analysis software (Shimadzu Corporation, Japan).

### Electrical measurement and characterization

A low-noise preamplifier (SR560, Stanford Research Systems, Sunnyvale, CA, USA) was employed to measure the output voltage of the triboelectric sensors. Applied pressure was monitored using a force sensor (Z2S-DPU-MZ-50N, IMADA, Toyohashi, Japan), while the compression frequency was varied from 0.25 to 2 Hz. Durability testing was performed by applying pressure at a constant frequency of 2 Hz, driven by a linear motor (WN500TA, Winner Optical Instruments, Beijing, China). Long-term stability was evaluated by measuring output voltage monthly over a 90-day period under the same testing conditions. Moisture resistance testing was accomplished by deploying the sensor within the oxygen mask and continuously wearing it at room temperature for 12 h, during which the electrical performance was monitored.

### Simulation of surface potential distribution

Finite element simulations were conducted using COMSOL Multiphysics (v. [6.3], COMSOL Inc., Stockholm, Sweden) to investigate the influence of surface roughness on triboelectric performance. Two-dimensional axisymmetric models were developed to represent smooth and rough electrode surfaces. The latter was characterized by a periodic array of isosceles triangles - with a base width of  $0.2\ \mu\text{m}$  and a height of  $0.1\ \mu\text{m}$  - consistent with the surface topography observed via atomic force microscopy (AFM) of plasma-treated fibers. Material properties for the epoxy resin and PVDF were sourced from the COMSOL built-in material library. Surface charge densities of  $\pm 3\ \mu\text{C}\cdot\text{m}^{-2}$  were applied to represent triboelectric charging, with opposite polarities assigned to the epoxy and PVDF surfaces. The contact-separation process was simulated by varying the electrode separation distance from  $0.1$  to  $5\ \mu\text{m}$  in  $0.1\ \mu\text{m}$  increments. The surface potential distribution was then derived from a steady-state calculation.

### Collection of respiratory data

Volunteers were fitted with pilot oxygen masks incorporating triboelectric sensors positioned above the mouth-nose airflow channel. Data acquisition was performed using an STM32 microcontroller (STMicroelectronics, Geneva, Switzerland) with a sampling rate of 100 Hz. Signal conditioning included amplification using an operational amplifier (OP07CP, Texas Instruments, Dallas, TX, USA) and low-pass filtering with a cutoff frequency of approximately 15.9 Hz to remove noise. The processed signals were then transmitted to the host computer via serial communication for further analysis.

### Feature extraction and classification of respiratory signals

Machine learning-based classification of respiratory patterns was implemented using a backpropagation neural network architecture based on features extracted from the respiratory signals. Feature extraction was performed in three domains to capture comprehensive characteristics of the respiratory signals. Time-domain features included breathing frequency, signal amplitude (representing breathing depth), inhalation time, exhalation time, and discrete signal energy calculated as the sum of squared voltage samples. Frequency-domain analysis employed the Fast Fourier Transform to determine the dominant frequency and its ratio to the total spectral power. Time-frequency domain features were extracted using the Short-Time Fourier Transform with a 512-sample window. The neural network consisted of an input layer with six neurons corresponding to the extracted features, two hidden layers with ten neurons each, and an output layer with six neurons representing the respiratory pattern classes. For network training, the Adam optimizer was adopted to optimize model parameters, and the cross-entropy loss function was used to quantify the discrepancy between predicted and true respiratory pattern labels. To enhance the model's generalization across subjects and its reliability for practical applications, a dataset of 5,500 labeled samples was compiled, collected from five distinct subjects and covering six target respiratory patterns. A portion of these samples was acquired under high electromagnetic field conditions and simulated flight-related stress, such as motion and vibration, to emulate interference in real flight environments. The dataset was partitioned to ensure unbiased performance evaluation: 5,000 samples were allocated to the training set, and the remaining 500 samples served as an independent held-out test set. The training set was further processed using five-fold stratified cross-validation to ensure robust model selection and hyperparameter tuning. The held-out test set was used exclusively for final performance evaluation to reflect the model's real-world predictive capability.

### Customized pilot respiratory monitoring user interface

A real-time monitoring interface was developed using the PyQt6 framework (Riverbank Computing, Dorchester, UK) to provide comprehensive visualization and analysis capabilities for pilot respiratory assessment. The interface integrated multiple display modules, including real-time waveform visualization, automated pattern classification results updated at the completion of each respiratory cycle, feature parameter tracking, and an alert management system for abnormal respiratory patterns.

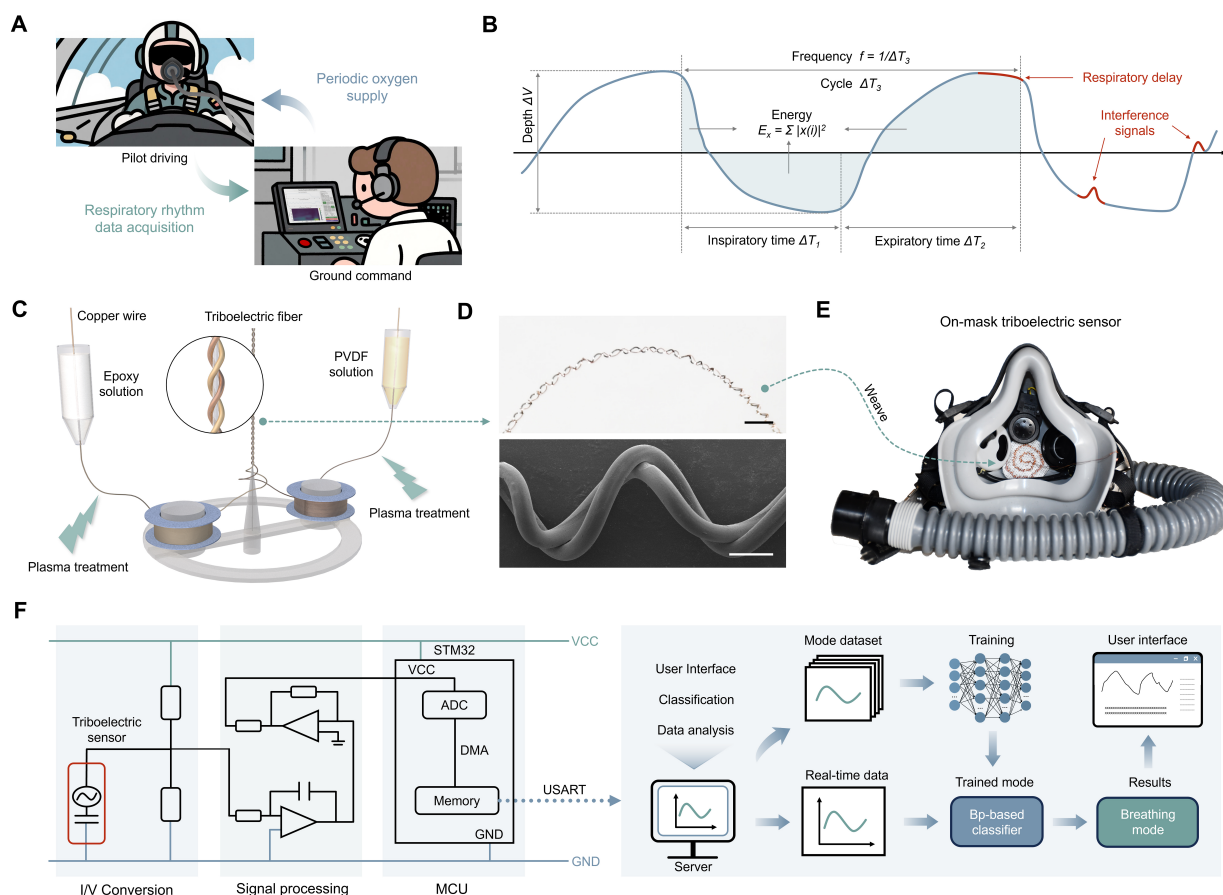


**Figure 1.** Design and preparation of respiratory monitoring system. (A) Schematic diagram of respiratory monitoring and oxygen supply between pilots and ground control platform; (B) Schematic diagram of periodic respiration waveform with feature extraction and artifact identification, including time, depth, energy, and frequency; (C) Fabrication process of triboelectric fibers; (D) (i) Digital image (Scale bar: 2 mm) and (ii) SEM image (Scale bar: 2  $\mu$ m) of triboelectric fibers; (E) Pilot mask integrated with triboelectric sensors; (F) Schematic illustration of the machine learning-assisted respiratory monitoring system. SEM: Scanning electron microscope; PVDF: polyvinylidene fluoride; VCC: voltage common collector; STM32: STMicroelectronics Microcontroller 32-bit; ADC: analog-to-digital converter; DMA: direct memory access; USART: universal synchronous asynchronous receiver transmitter; GND: ground; MCU: microcontroller unit.

## RESULTS AND DISCUSSION

### Design and fabrication of the respiratory monitoring system

To address the needs of extreme scenarios, the sensor system is designed in a form that can be placed inside the breathing mask to enable real-time, non-invasive monitoring of respiratory parameters. This configuration enables unobtrusive placement within standard respiratory protection gear, allowing continuous monitoring without impeding the wearer. Figure 1A demonstrates a potential application involving a high-altitude fighter pilot equipped with a sensor-integrated oxygen mask that continuously monitors respiratory patterns and transmits data to a ground station. It captures periodic respiratory waveforms while extracting key features and identifying artifacts for respiratory assessment, as schematically illustrated in Figure 1B. When the system detects respiratory abnormalities, the monitoring system can trigger an alarm promptly to assist the command center in quickly adjusting the oxygen supply strategy and ensuring pilot safety. Thus, fast detection and clear alarms are essential to timely interventions in mission-critical environments. Such mission-critical operation demands exceptional sensitivity and robust performance under dynamic motion and low-pressure conditions.

The core sensing element is composed of plasma-treated triboelectric fibers fabricated through a multi-step

process [Figure 1C]. Copper wires, respectively coated with epoxy resin and PVDF, form the triboelectric pair [Supplementary Figure 1]. To enhance the sensitivity of the triboelectric sensor<sup>[40]</sup>, we employ a plasma surface treatment using a 1:1 argon-oxygen gas mixture under low pressure [Supplementary Note 1], which modifies the fiber surface by creating nanoscale roughness and surface modification<sup>[41,42]</sup>. These wires are then helically twisted into flexible yarns and woven into textiles [Supplementary Figure 2]. The macroscopic and scanning electron microscopy images of the resulting textiles reveal a uniform fiber arrangement with consistent coating [Figure 1D]. These images confirm the micro- and nanoscale surface features introduced by plasma treatment and the uniformity of the coatings, which together underpin consistent sensor performance. When positioned above the mouth-nose airflow channel of a fighter-pilot oxygen mask [Figure 1E], cyclic inhaled and exhaled airflow deforms the textile, generating periodic triboelectric voltage signals<sup>[43–45]</sup>. These voltage signals are subsequently acquired and processed by a machine learning-assisted monitoring system, including feature extraction, respiratory patterns classification, and real-time breathing metrics display to support adaptive oxygen delivery [Figure 1F].

### Characterization of surface-modified triboelectric fibers

During the plasma treatment, high-energy ions bombard the polymer surface, causing surface roughness to increase the frictional contact area between fibers for enhanced signal output intensity from small deformations [Figure 2A]<sup>[42,46]</sup>. To establish a clear link between processing parameters and sensor performance, we systematically characterized both morphology and chemistry of the fibers after different plasma exposure durations. Figure 2B and C shows the surface-treated epoxy-coated and PVDF-coated copper wires. These macroscopic images provide preliminary visual confirmation of the surface coating on the copper wires. Figure 2D and E confirms significant morphological changes after 60-minute plasma treatment. The untreated fibers exhibit relatively smooth surfaces [Figure 2D<sub>I</sub>, 2D<sub>II</sub>, 2E<sub>I</sub>, and 2E<sub>II</sub>], while the plasma-treated fibers develop pronounced nanoscale roughness with characteristic etching patterns [Figure 2D<sub>III</sub>, 2D<sub>IV</sub>, 2E<sub>III</sub>, and 2E<sub>IV</sub>]. The contrast between untreated and treated surfaces indicates that plasma processing effectively creates new topographical features that are expected to increase effective contact area during mechanical deformation. Moreover, EDS mappings [Supplementary Figures 3–5] show the compositional changes of carbon, oxygen, and fluorine elements on the surfaces of epoxy resin and PVDF fibers. Progressive surface modifications are observed with increasing plasma treatment duration [Supplementary Figures 6 and 7]. Three-dimensional AFM further confirms the enhancement in surface roughness after plasma treatment [Figure 2F and Supplementary Figure 8]. Quantitative analysis of surface roughness parameters, including  $R_a$  and  $R_q$  demonstrates a significant increase with plasma treatment duration [Figure 2G].

Chemical changes are characterized using FTIR spectroscopy. Figure 2H presents the FTIR spectra of epoxy and PVDF fibers before and after 60-minute plasma treatment, respectively. For epoxy fibers [Figure 2H<sub>I</sub>], the plasma treatment introduced oxygen-containing groups. These modifications are evidenced by the enhanced absorption around  $1,200\text{ cm}^{-1}$ , where the C–O stretching vibrations become more pronounced. Additionally, the characteristic C–H stretching vibration at  $2,900\text{ cm}^{-1}$  shows reduced intensity after treatment, indicating that the introduced oxide leads to the removal or oxidation of C–H groups. For epoxy fibers [Figure 2H<sub>II</sub>], plasma treatment resulted in the disappearance of minor absorption peaks in the  $1,500\text{--}1,600\text{ cm}^{-1}$  region, which correspond to the stretching vibration of C=C bonds in the aromatic ring and the bending vibration of C–H bonds. Besides, the weakened C–H stretching vibrations around  $2,900\text{ cm}^{-1}$  corresponding to non-polar aliphatic groups (methyl and methylene) manifest as a notable reduction in absorption intensity. This can also be attributed to surface damage and coverage of oxygen-containing functional groups. XPS analysis of the C 1s spectra further confirmed the plasma-induced surface chemical modifications of PVDF and epoxy fibers [Supplementary Figure 9]. For PVDF, the C–C, CH<sub>2</sub>, and CF/C–F components shift from 284.0, 285.3, and 288.0 eV to 284.2, 286.4, and 291.3 eV, respectively. The binding



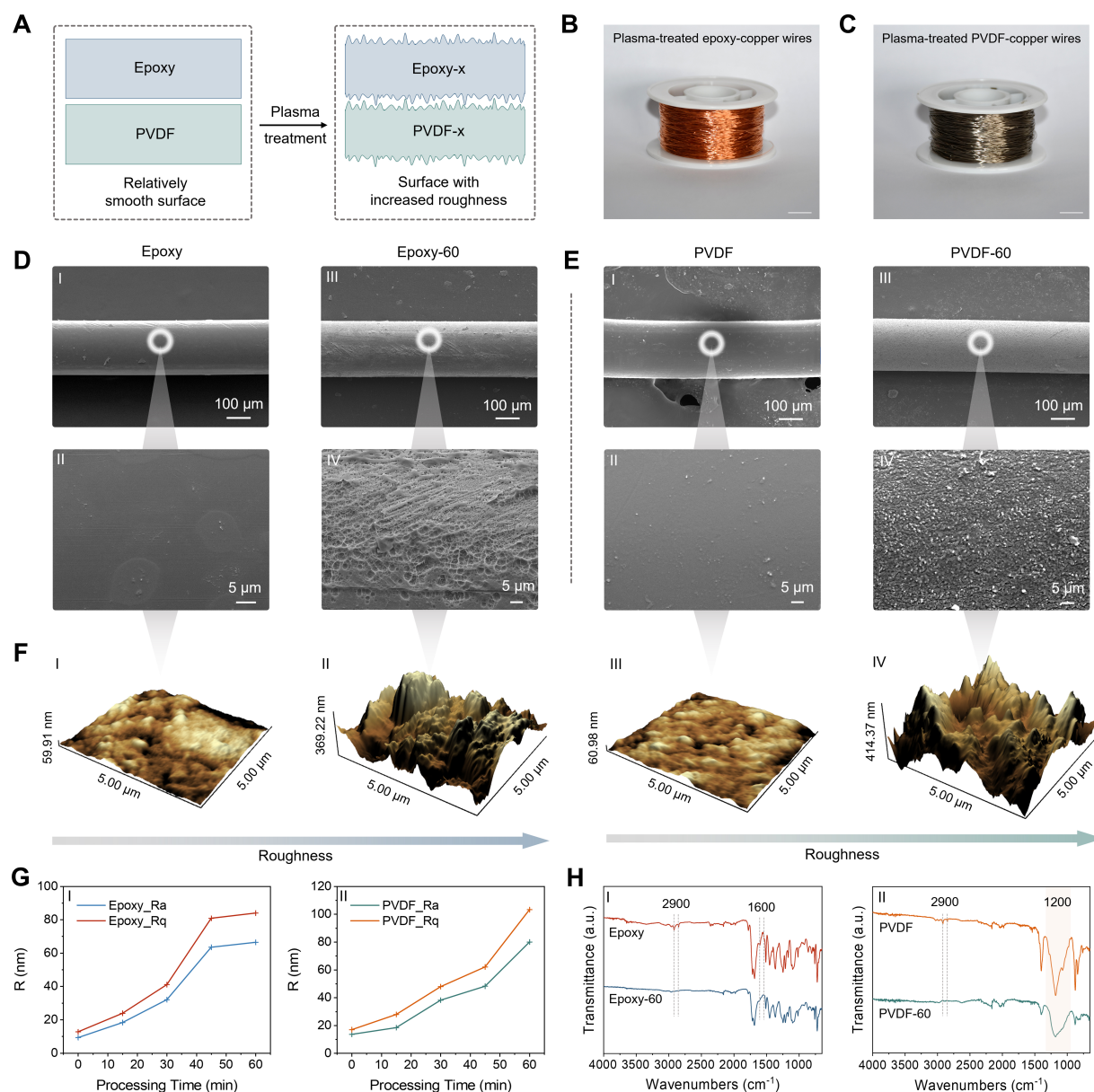


**Figure 2.** Characterization of the surface treatment of triboelectric fibers. (A) Schematic illustration of the fiber surfaces before and after plasma treatment. Digital images of surface-treated (B) epoxy-coated and (C) PVDF-coated copper wires with a diameter of 200 μm (Scale bar: 10 mm); (D) and (E) SEM images, and (F) 3D AFM images of epoxy and PVDF fibers before and after 60-minute plasma treatment, respectively; (G) Roughness variation of 5 μm × 5 μm surface regions for epoxy and PVDF fibers with plasma treatment time at varying durations; (H) FTIR spectra of epoxy and PVDF fibers before and after plasma treatment. PVDF: Polyvinylidene fluoride; SEM: scanning electron microscope; 3D: three-dimensional; AFM: atomic force microscopy; FTIR: Fourier Transform Infrared.

energy increases are mainly attributed to surface defluorination, which removes the strong shielding effect of fluorine, and to concurrent oxidation that introduces electronegative oxygen species; both effects reduce the electron density at carbon sites. For the epoxy resin, the C–C/C–H, C–O and C=O/O–C components shift from 284.2, 285.3 and 288.2 eV to 285.0, 286.0 and 289.2 eV, respectively. The upward shifts are consistent with substantial near-surface oxidation that replaces C–H bonds with more electronegative C–O bonds, thereby lowering the electron cloud density on the carbon atoms. These systematic shifts to higher binding energy confirm that plasma treatment significantly modified the surface chemistry of both materials.



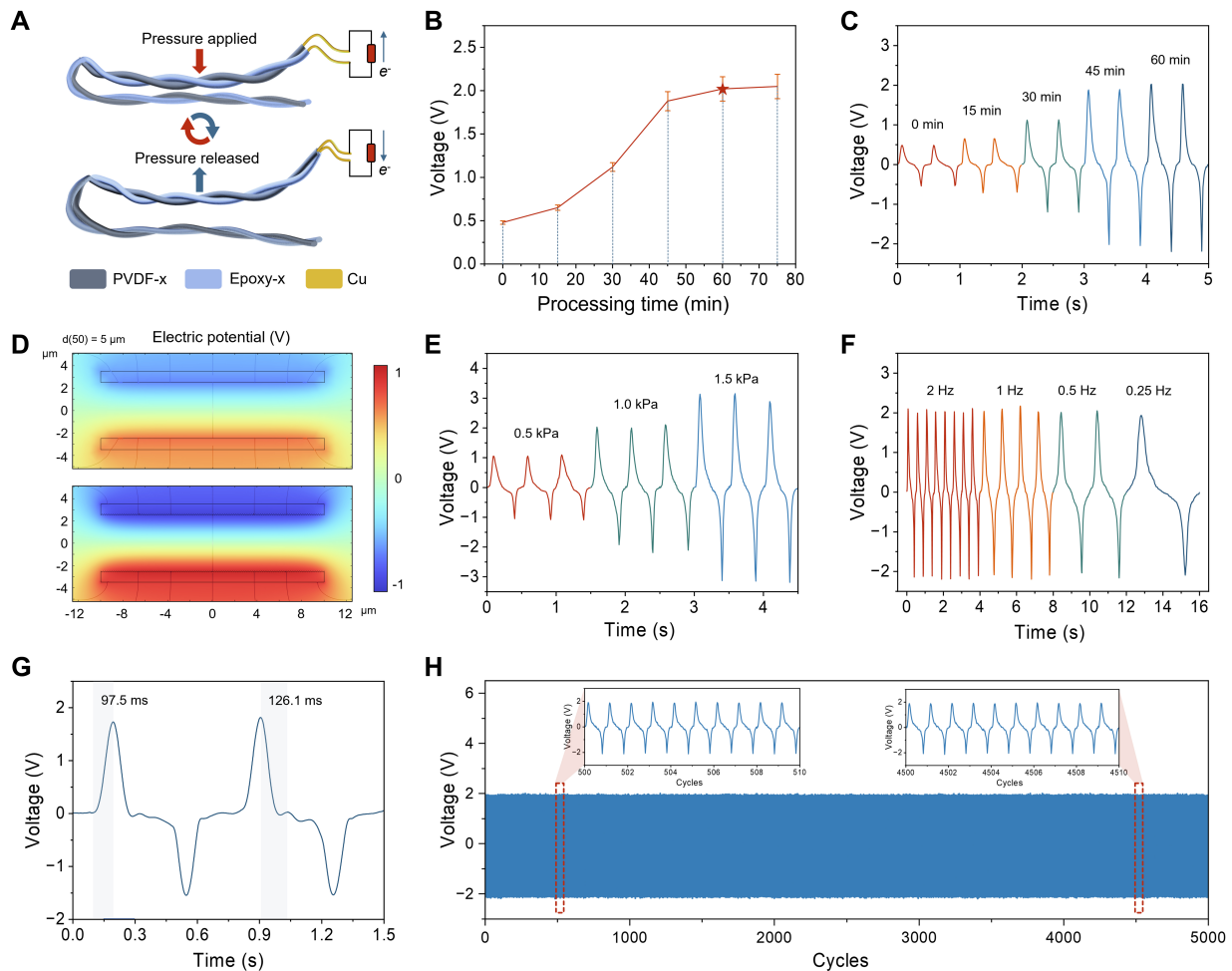


**Figure 3.** Electrical properties of the respiratory triboelectric sensors. (A) Schematic diagram of the working mechanism; (B) Output voltages comparison and (C) Signal output curves of sensors with different plasma treatment times under an external pressure of 1 kPa; (D) Simulation mappings of surface potential distribution during contact-separation process for smooth-surfaced and rough-surfaced fibers; (E) and (F) Output curves of the respiratory triboelectric sensors under different pressures at a constant frequency of 2 Hz and under different frequencies at a constant pressure of 1 kPa, respectively; (G) Response and recovery times of the respiratory triboelectric sensor; (H) Durability test of the respiratory triboelectric sensor under a pressure of 1 kPa. PVDF: Polyvinylidene fluoride.

### Electrical properties of triboelectric respiratory sensors

The working mechanism of the respiratory triboelectric sensor is based on the coupling of contact electrification [Supplementary Figure 10] and electrostatic induction [Supplementary Figure 11]<sup>[47–49]</sup>. During inhalation and exhalation, the airflow-induced deformation causes periodic contact and separation between the epoxy and PVDF fibers [Figure 3A]<sup>[50,51]</sup>. Upon contact, electrons transfer from the epoxy to the PVDF due to their difference in electron affinity, creating opposite triboelectric charges on their surfaces. During separation, the charge redistribution induces a potential difference, driving electrons to flow through the external circuit. This cyclic process generates alternating electrical signals that correspond to the respiratory rhythm. Thus, the sensor transduces the mechanical waveform of breathing into time-resolved electrical signals that can be directly correlated with respiratory metrics.

To optimize sensor performance, the effect of plasma treatment duration on output voltage is investigated to establish a direct processing-performance relationship. Figure 3B presents a comparative analysis of the output voltage of triboelectric sensors under a consistent external pressure of 1 kPa for varying plasma treatment durations. The output voltage increased with plasma treatment time, reaching an optimal point at

60 min, which represents approximately 420% enhancement ( $2.05 \pm 0.14$  V) compared to the untreated sensor ( $0.48 \pm 0.02$  V). This dramatic increase highlights the critical role of nanoscale surface engineering in amplifying triboelectric electricity generation. Representative output voltage waveforms for sensors with different plasma treatment times confirm consistent improvement in signal amplitude [Figure 3C]. Simulation results further validate the impact of surface roughness on triboelectric performance. Finite element simulations of the surface potential distribution during the contact-separation process for both smooth-surfaced and rough-surfaced devices indicate that the increased surface roughness leads to enhanced open-circuit voltage [Figure 3D and Supplementary Figure 12]. Long-term cyclic stability under repeated deformation demonstrates the suitability of the textile sensor for continuous, real-world respiratory monitoring.

Sensor sensitivity is evaluated by measuring output voltage under varying pressures (from 0.5 to 1.5 kPa) at a constant 2 Hz frequency [Figure 3E] and varying frequencies (from 2 to 0.25 Hz) at a constant 1 kPa pressure [Figure 3F]. The results demonstrate a linear response to pressure changes with a sensitivity of  $2.02 \text{ V} \cdot \text{kPa}^{-1}$  and stable performance across frequencies, indicating reliability for respiratory monitoring. The response and recovery times of the triboelectric sensor are measured to be 96 and 126.1 ms [Figure 3G], which enables the detection of transient respiratory events and abrupt changes in breathing patterns that may indicate physiological distress. Moreover, the textile sensor demonstrates outstanding durability, maintaining stable output performance over 5,000 continuous operating cycles [Figure 3H]. Collectively, the experimental measurements and simulations show that controlled plasma-induced nanoscale roughness is a practical and effective strategy to enhance triboelectric output for reliable respiratory monitoring.

### On-mask triboelectric sensors for respiratory monitoring

The system implementation involves continuous monitoring and analysis of respiratory parameters from testers wearing the sensor-integrated mask in real-world scenarios [Figure 4A and Supplementary Figure 13] and simulated strong electromagnetic field environments. The triboelectric sensor produces distinctive voltage signals corresponding to various respiratory patterns in real-world scenarios, including normal, rapid, deep, shallow, speaking, and dyspneic breathing [Figure 4B]. Each pattern generates a unique waveform with characteristic features in terms of amplitude, frequency, and regularity, which forms the basis for subsequent signal analysis and machine learning-driven classification. Even in strong electromagnetic field environments, the high-frequency noise in raw sensor signals can be effectively filtered by our custom hardware low-pass circuit [Supplementary Figure 14], confirming the system's robustness against electromagnetic interference [Supplementary Figure 15]. Figure 4C shows the correspondence between the signal curve and the stages of exhalation and inhalation during normal breathing. This mapping verifies that temporal features of the voltage trace accurately reflect physiological respiratory phases. In comparison, Figure 4D shows the signal curve output by abnormal breathing caused by interference signals, and breathing delays can be sensitively detected. Interference signals introduced by mechanical actions during actual use are identified by a custom algorithm, which analyzes the temporal continuity and amplitude variation characteristics of respiratory signals. Breathing delays are distinguished by the characteristics of the inspiratory phase following exhalation: normal breathing shows a rapid downward transition, while breathing delay presents a gradual decrease. The extraction of these features provides a guarantee for the accurate classification of subsequent dynamic breathing patterns.

To ensure reliable performance under extreme conditions, we assess the electrical durability of the triboelectric sensor during prolonged use [Figure 4E]. Long-term testing reveals that the sensor retains over 95% of its initial output voltage after 90 days of regular use, indicating excellent durability for practical applications. Besides, stable output under humid conditions is critical for long-lasting scenarios. We conducted a 12-hour continuous wear test with sensor-integrated masks [Figure 4F], where the sensor was in

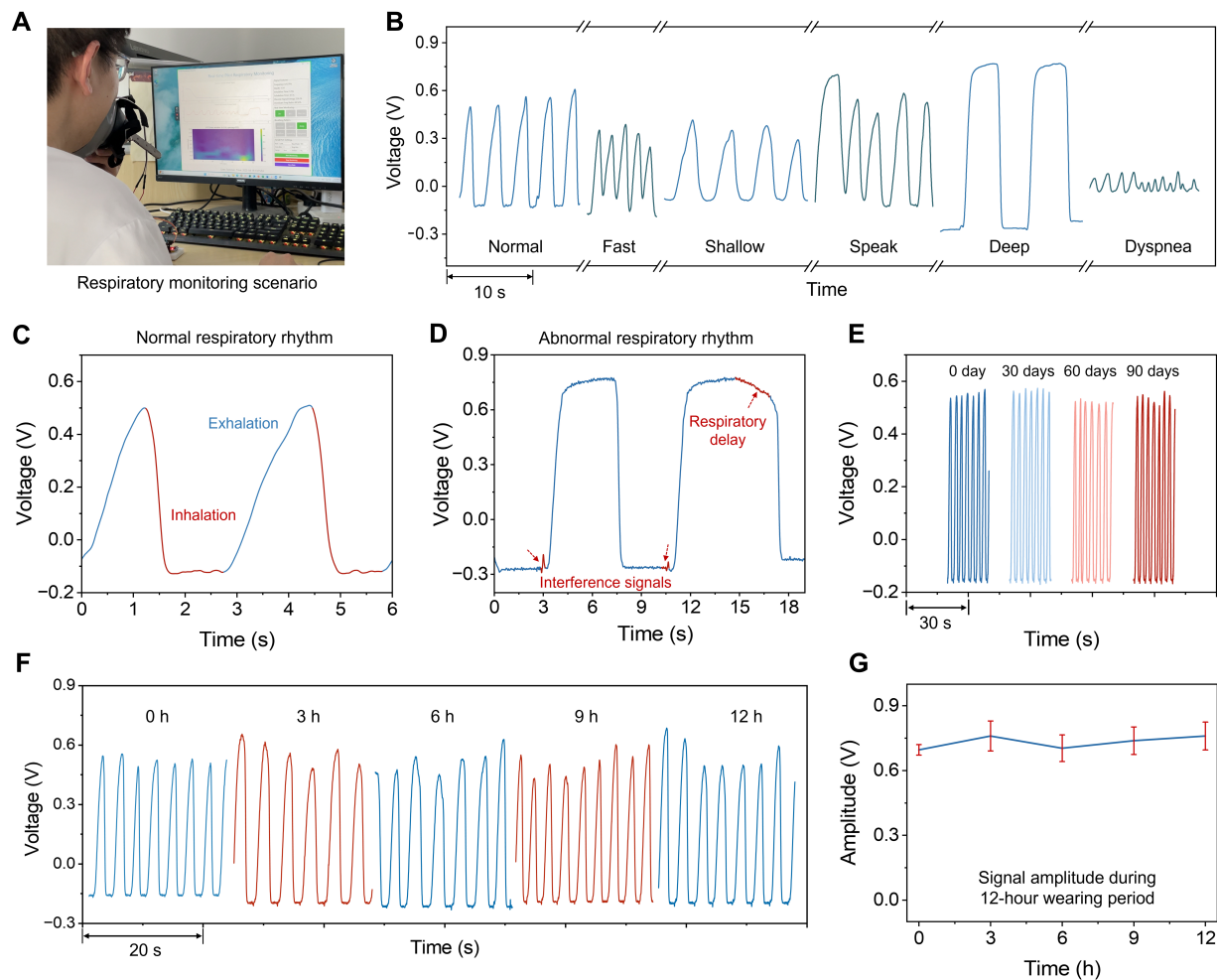


**Figure 4.** Stability characterization of triboelectric sensors for dynamic respiratory monitoring. (A) Digital image of the simulated respiratory monitoring scenario; (B) Output signals under different respiratory patterns; (C) Algorithmic identification of exhalation/inhalation phases in measured respiratory signal; (D) Algorithmic identification of interference and respiration delay in respiratory signals; (E) Output voltage signal of the sensor over a period of 90 days; (F) Output voltage of textile sensor after mask wearing within 12 h; (G) Amplitude variation curve within 12 h.

direct contact with exhaled vapor, and volunteers performed strenuous exercise midway to simulate sweating. The sensor maintained stable output performance over 12 h of continuous wear, demonstrating its suitability for extended flight [Figure 4G]. The results of long-term stability and moisture-resistance tests indicate that the integrated system is both robust and practical for in-flight respiratory monitoring, supporting timely pilot assessment and adaptive oxygen management.

### Machine learning-enabled real-time respiratory monitoring system

To demonstrate the practical utility of the triboelectric respiratory sensor, we develop a machine learning-assisted real-time monitoring system for pilot respiratory assessment. The signal processing and analysis system is outlined in Figure 5A. Raw voltage signals are processed by filtering and amplification before being acquired by a microcontroller unit and transmitted to a host computer. Feature extraction is then performed in three domains [Supplementary Note 2] of the time domain (frequency, depth, inhalation time, exhalation time, and discrete signal energy), frequency domain (dominant frequency ratio), and time-frequency domain (Short-Time Fourier Transform). These multimodal features serve as inputs to a backpropagation neural network, selected after comparing with several other machine learning modules [Supplementary Table 1]. The machine learning model is trained and validated using 5,000 annotated

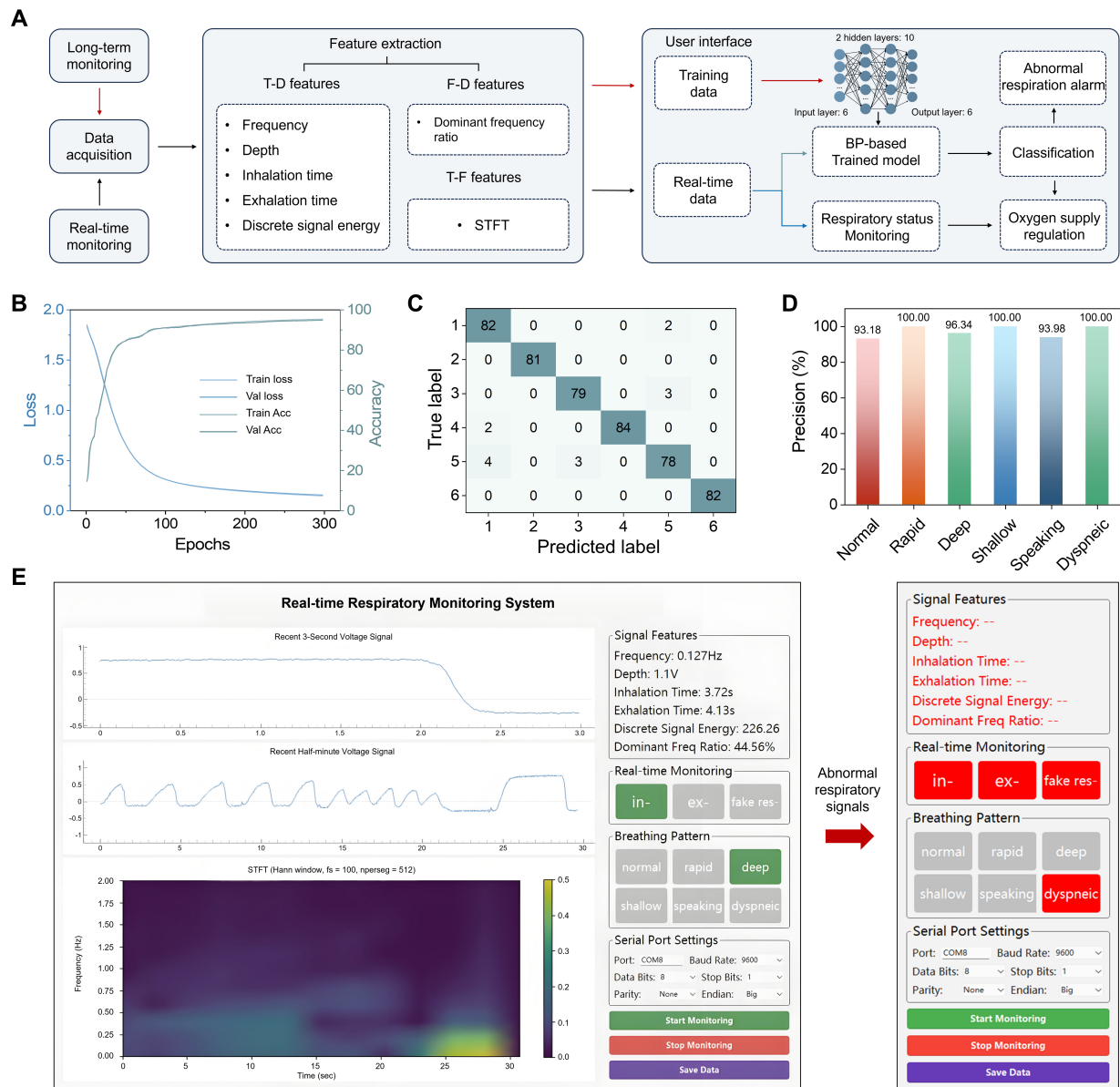


**Figure 5.** Application of the machine learning-assisted real-time pilot respiratory monitoring system. (A) Schematic diagram of the respiratory monitoring and signal processing system; (B) Loss function and accuracy for the training and validation sets over 300 epochs; (C) Confusion matrix for the classification of 6 respiratory patterns, where Labels 1–6 correspond to normal, rapid, deep, shallow, speaking, and dyspneic breath, respectively; (D) Classification precision of 6 respiratory patterns; (E) User interface for the real-time pilot respiratory monitoring system. T-D: Time-domain; F-D: frequency-domain; T-F: time-frequency; STFT: short-time Fourier transform; BP: back propagation; Acc: accuracy.

respiratory segments acquired from long-term monitoring, with the loss function decreasing below 0.15 and validation accuracy exceeding 95% after 300 epochs [Figure 5B]. The final model achieves an overall accuracy of 97.2% in classifying the six respiratory patterns and maintains excellent real-time performance to meet the demands of on-mask respiratory monitoring, with an average classification time of 0.157 milliseconds per sample on the test set. The classification results [Figure 5C and Supplementary Figure 16] demonstrate the excellent performance across all pattern categories, with precision values exceeding 93% for each respiratory pattern and 100% for three patterns [Figure 5D].

Ultimately, a real-time monitoring user interface is integrated to provide continuous visualization of

respiratory waveforms, automated pattern classification results, and analysis of signal features [Figure 5E]. The interface offers both summary dashboards and event-level detail to support rapid decision-making by flight personnel or ground operators. When the automatic pattern classification results in ‘dyspneic respiration’, the system automatically triggers alerts [Supplementary Figure 17], enabling prompt intervention in potential hypoxia or respiratory distress scenarios. An algorithmic analysis of the descending slope also allows the system to identify inhalation and exhalation phases and distinguish between genuine respiratory signals and artifacts caused by breath-holding, thereby providing a foundation for oxygen supply regulation in the mask. This integration enables adaptive life support control based on classified respiratory patterns, enhancing pilot safety during high-altitude operations where rapid physiological changes can have serious consequences. In summary, the combined signal-processing, classification, and user-interface components produce a closed-loop monitoring solution that is accurate, timely, and suited for critical mission respiratory support.

## CONCLUSIONS

In summary, we developed a machine learning-assisted real-time and high-sensitivity respiratory dynamics monitoring system designed for deployment in demanding extreme scenarios to ensure continuous, high-fidelity assessment of breathing patterns. To enhance the sensitivity of the triboelectric sensor, we apply plasma treatment to triboelectric fibers sewn into a flexible textile and embedded in a standard oxygen mask. This approach yields a response time of 96 ms, a sensitivity of  $2.02 \text{ V} \cdot \text{kPa}^{-1}$ , and a 420% increase in output voltage. A miniaturized acquisition module performs multimodal feature extraction and intelligent algorithm-driven classification of six respiratory patterns with 97.2% accuracy, enabling precise discrimination of authentic breathing signals from artifacts such as speech or coughing. This integrated platform provides continuous, accurate tracking of respiratory parameters without compromising comfort or mask functionality, achieving superior sensitivity and wearability compared with prior art. It therefore supplies critical decision-support data for adaptive oxygen regulation and ground command systems in aviation, critical care, and telemedicine applications.

## DECLARATIONS

### Acknowledgments

The authors thank Ms. He Dan at the National Innovation Platform for Industry-Education Integration of Energy Storage Technology, Xi'an Jiaotong University, for her support with the XPS tests. The authors also thank Ms. Guo Hang at the Instrument Analysis Center of Xi'an Jiaotong University for assistance with SEM and AFM analyses.

### Authors' contributions

Conceived the research and supervised all aspects of the work: Fang, Y.; Xu, F.; Gan, J.

Provided the physiological characteristics of respiratory dynamics under extreme conditions: Wang, J.; Lin, T.

Discussed the device structure and fabrication: Zhao, J.; Pan, X.; Gan, J.

Fabricated the textile triboelectric sensor, conducted the measurements, simulated the electric potential distributions, and analyzed the raw data: Zhao, J.; Pan, X.; Yuan, M.; Long, Y.; Niu, Y.

Conducted the machine learning for respiratory pattern recognition: Zhao, J.; Sun, Y.

Designed the wireless pulse monitoring system and developed the ‘*Real-time Respiratory Monitoring System*’ APP program: Zhao, J.

Prepared the manuscript: Zhao, J.; Pan, X.

Zhao, J. and Pan, X. contributed equally to this work. All of the authors read, edited, and approved the final version of the manuscript.

### Availability of data and materials

The data that support the findings of this study are available from the corresponding author upon reasonable request.



### Financial support and sponsorship

This work was supported by the Aeronautics Science Foundation Program (ASFC-20240029070001), the National Natural Science Foundation of China (62201446), the Young Talent Support Plan of Xi'an Jiaotong University (0020220023), and the Medicine-Engineering Interdisciplinary Research Program (YGJC202207 and YGJC202208).

### Conflicts of interest

Gan, J. is affiliated with Avic Aerospace Life-Support Industries, LTD., while the other authors have declared that they have no conflicts of interest.

### Ethical approval and consent to participate

This study adhered to local regulations and ethical standards, involving exclusively non-invasive monitoring of body movements and physiological signals. Since no sensitive personal data were collected and the procedures involved no commercial interests or risk of participant harm, the study was deemed exempt from formal ethical review. All signal tests involving human subjects were conducted with the informed consent of the participants, who are also co-authors of this study.

### Consent for publication

The participants involved in the study have provided informed consent for the publication of any potentially identifying images.

### Copyright

© The Author(s) 2026.

## REFERENCES

1. Shen, S.; Zhou, Q.; Chen, G.; et al. Advances in wearable respiration sensors. *Mater. Today*. **2024**, *72*, 140–62. DOI
2. Negro CA, Funk GD, Feldman JL. Breathing matters. *Nat. Rev. Neurosci.* **2018**, *19*, 351–67. DOI PubMed PMC
3. Rodrigues V, Pratt RA, Stephens CL, Alexander DJ, Napoli NJ. Work of breathing for aviators: a missing link in human performance. *Life* **2024**, *14*, 1388. DOI PubMed PMC
4. Soh, M. S.; Jang, J. H.; Park, J. S.; Shin, J. H. Effects of high-gravity acceleration forces and anti-gravity maneuver on the cardiac function of fighter pilots. *Sci. Rep.* **2024**, *14*, 8749. DOI PubMed PMC
5. Petraki, K.; Grammatikopoulou, M. G.; Tekos, F.; et al. Estimation of redox status in military pilots during hypoxic flight-simulation conditions—a pilot study. *Antioxidants* **2022**, *11*, 1241. DOI PubMed PMC
6. Chen, G.; Shen, S.; Tat, T.; et al. Wearable respiratory sensors for COVID-19 monitoring. *View* **2022**, *3*, 20220024. DOI PubMed PMC
7. Geng, M.; Zhao, J.; Li, J.; et al. Facilitating response/recovery of cellulosic humidity sensor by densifying fibril arrays. *Chem. Eng. J.* **2024**, *500*, 157221. DOI
8. Geng, M.; Pan, X.; Zhao, J.; et al. Regulating crystal growth of Cs<sub>2</sub>SnCl<sub>6</sub> perovskite for rapid response and durable humidity-triggered non-contact sensor. *Chem. Eng. J.* **2024**, *486*, 150222. DOI
9. Vicente, B. A.; Sebastião, R.; Sencadas, V. Wearable devices for respiratory monitoring. *Adv. Funct. Mater.* **2024**, *34*, 2404348. DOI
10. Chen, G.; Xiao, X.; Zhao, X.; Tat, T.; Bick, M.; Chen, J. Electronic textiles for wearable point-of-care systems. *Chem. Rev.* **2022**, *122*, 3259–91. DOI PubMed
11. Fang, Y.; Chen, G.; Bick, M.; Chen, J. Smart textiles for personalized thermoregulation. *Chem. Soc. Rev.* **2021**, *50*, 9357–74. DOI PubMed
12. Libanori, A.; Chen, G.; Zhao, X.; Zhou, Y.; Chen, J. Smart textiles for personalized healthcare. *Nat. Electron.* **2022**, *5*, 142–56. DOI
13. Sheng, F.; Zhao, C.; Zhang, B.; Tan, Y.; Dong, K. Flourishing electronic textiles towards pervasive, personalized and intelligent healthcare. *Soft. Sci.* **2024**, *4*, 2. DOI
14. Ahn, S.; Cho, Y.; Park, S.; et al. Wearable multimode sensors with amplified piezoelectricity due to the multi local strain using 3D textile structure for detecting human body signals. *Nano. Energy*. **2020**, *74*, 104932. DOI
15. Wang, X.; Xiao, X.; Feng, Z.; Wu, Y.; Yang, J.; Chen, J. A soft bioelectronic patch for simultaneous respiratory and cardiovascular monitoring. *Adv. Healthc. Mater.* **2024**, *13*, e2303479. DOI PubMed
16. Wu, Y.; Wu, Y.; Menon, C. Screen-printing tribovoltaic textile with enhanced interface layer for motion tracking and respiration monitoring. *Nano. Energy*. **2025**, *141*, 111095. DOI

17. Liu, Z.; Zhao, Z.; Zeng, X.; Fu, X.; Hu, Y. Expandable microsphere-based triboelectric nanogenerators as ultrasensitive pressure sensors for respiratory and pulse monitoring. *Nano. Energy*. **2019**, *59*, 295–301. [DOI](#)
18. Liang, Y.; Ding, Q.; Wang, H.; et al. Humidity sensing of stretchable and transparent hydrogel films for wireless respiration monitoring. *Nanomicro. Lett.* **2022**, *14*, 183. [DOI PubMed PMC](#)
19. Ni, X.; Ouyang, W.; Jeong, H.; et al. Automated, multiparametric monitoring of respiratory biomarkers and vital signs in clinical and home settings for COVID-19 patients. *Proc. Natl. Acad. Sci. U. S. A.* **2021**, *118*, e2026610118. [DOI PubMed PMC](#)
20. Liu, J.; Wang, H.; Liu, T.; et al. Multimodal hydrogel-based respiratory monitoring system for diagnosing obstructive sleep apnea syndrome. *Adv. Funct. Mater.* **2022**, *32*, 2204686. [DOI](#)
21. Zhao, W.; He, P.; Ling, K.; et al. Printed graphene/CNTs/TPU-fabric wearable strain sensor for healthcare monitoring. *Soft. Sci.* **2025**, *5*, 10. [DOI](#)
22. Dinh, T.; Nguyen, T.; Phan, H. P.; Nguyen, N. T.; Dao, D. V.; Bell, J. Stretchable respiration sensors: advanced designs and multifunctional platforms for wearable physiological monitoring. *Biosens. Bioelectron.* **2020**, *166*, 112460. [DOI PubMed](#)
23. Menden, T.; Alcaín, G. B.; Stevenson, A. T.; et al. Dynamic lung behavior under high G acceleration monitored with electrical impedance tomography. *Physiol. Meas.* **2021**, *42*, 094001. [DOI PubMed](#)
24. Yan, M.; Hao, Q.; Diao, S.; et al. Smart home sleep respiratory monitoring system based on a breath-responsive covalent organic framework. *ACS. Nano*. **2024**, *18*, 728–37. [DOI PubMed](#)
25. Qin, J.; Yang, X.; Shen, C.; et al. Carbon nanodot-based humidity sensor for self-powered respiratory monitoring. *Nano. Energy*. **2022**, *101*, 107549. [DOI](#)
26. Pang, Y.; Jian, J.; Tu, T.; et al. Wearable humidity sensor based on porous graphene network for respiration monitoring. *Biosens. Bioelectron.* **2018**, *116*, 123–9. [DOI PubMed](#)
27. Lei, D.; Zhang, Q.; Liu, N.; et al. Self-powered graphene oxide humidity sensor based on potentiometric humidity transduction mechanism. *Adv. Funct. Mater.* **2022**, *32*, 2107330. [DOI](#)
28. Mandal, S.; Mantilla, H. M.; Loganathan, K.; et al. Ultra-fast moisture sensor for respiratory cycle monitoring and non-contact sensing applications. *Adv. Mater.* **2025**, *37*, e2414005. [DOI PubMed PMC](#)
29. Xu, Z.; Hao, Y.; Luo, A.; Jiang, Y. Technologies and applications in wireless biosensors for real-time health monitoring. *Med-X* **2024**, *2*, 41. [DOI](#)
30. Zhou, B.; Ding, L.; Chen, B.; et al. Physiological characteristics and operational performance of pilots in the high temperature and humidity fighter cockpit environments. *Sensors* **2021**, *21*, 5798. [DOI PubMed PMC](#)
31. Zhang, Q.; Soham, D.; Liang, Z.; Wan, J. Advances in wearable energy storage and harvesting systems. *Med-X* **2025**, *3*, 48. [DOI](#)
32. Kwak, W.; Yin, J.; Wang, S.; Chen, J. Advances in triboelectric nanogenerators for self-powered wearable respiratory monitoring. *FlexMat* **2024**, *1*, 5–22. [DOI](#)
33. Su, Y.; Chen, G.; Chen, C.; et al. Self-powered respiration monitoring enabled by a triboelectric nanogenerator. *Adv. Mater.* **2021**, *33*, e2101262. [DOI PubMed](#)
34. Dai, J.; Li, L.; Shi, B.; Li, Z. Recent progress of self-powered respiration monitoring systems. *Biosens. Bioelectron.* **2021**, *194*, 113609. [DOI PubMed](#)
35. Tat, T.; Libanori, A.; Au, C.; Yau, A.; Chen, J. Advances in triboelectric nanogenerators for biomedical sensing. *Biosens. Bioelectron.* **2021**, *171*, 112714. [DOI PubMed](#)
36. Li, J.; Long, Y.; Yang, F.; Wang, X. Respiration-driven triboelectric nanogenerators for biomedical applications. *EcoMat* **2020**, *2*, e12045. [DOI PubMed PMC](#)
37. Fang, Y.; Zou, Y.; Xu, J.; et al. Ambulatory cardiovascular monitoring via a machine-learning-assisted textile triboelectric sensor. *Adv. Mater.* **2021**, *33*, e2104178. [DOI PubMed PMC](#)
38. Ates, H. C.; Nguyen, P. Q.; Gonzalez-Macia, L.; et al. End-to-end design of wearable sensors. *Nat. Rev. Mater.* **2022**, *7*, 887–907. [DOI PubMed PMC](#)
39. Lee, Y. J.; Park, C.; Kim, H.; Cho, S. J.; Yeo, W. Artificial intelligence on biomedical signals: technologies, applications, and future directions. *Med-X* **2024**, *2*, 43. [DOI](#)
40. Lone, S. A.; Lim, K. C.; Kaswan, K.; et al. Recent advancements for improving the performance of triboelectric nanogenerator devices. *Nano. Energy*. **2022**, *99*, 107318. [DOI](#)
41. Li, C.; Yang, Y.; Qu, R.; et al. Recent advances in plasma etching for micro and nano fabrication of silicon-based materials: a review. *J. Mater. Chem. C*. **2024**, *12*, 18211–37. [DOI](#)
42. Xiao, K.; Wang, W.; Wang, K.; Zhang, H.; Dong, S.; Li, J. Improving triboelectric nanogenerators performance via interface tribological optimization: a review. *Adv. Funct. Mater.* **2024**, *34*, 2404744. [DOI](#)
43. Liu, J.; Gu, L.; Cui, N.; Xu, Q.; Qin, Y.; Yang, R. Fabric-based triboelectric nanogenerators. *Research* **2019**, *2019*, 1091632. [DOI PubMed PMC](#)

- 
44. Seidi, F.; Deng, C.; Zhong, Y.; et al. Functionalized masks: powerful materials against COVID-19 and future pandemics. *Small* **2021**, *17*, e2102453. [DOI PubMed PMC](#)
  45. Kim, W. G.; Kim, D. W.; Tcho, I. W.; Kim, J. K.; Kim, M. S.; Choi, Y. K. Triboelectric nanogenerator: structure, mechanism, and applications. *ACS. Nano.* **2021**, *15*, 258-87. [DOI PubMed](#)
  46. Ahmed, A. A.; Qahtan, T. F.; Afzal, N.; Rashid, M.; Thalluri, L. N.; Mohamed, Ali. M. S. Low-pressure air plasma-treated polytetrafluoroethylene surface for efficient triboelectric nanogenerator. *Mater. Today. Sustain.* **2023**, *21*, 100330. [DOI](#)
  47. Chen, G.; Li, Y.; Bick, M.; Chen, J. Smart textiles for electricity generation. *Chem. Rev.* **2020**, *120*, 3668-720. [DOI PubMed](#)
  48. Chen, J.; Huang, Y.; Zhang, N.; et al. Micro-cable structured textile for simultaneously harvesting solar and mechanical energy. *Nat. Energy.* **2016**, *1*, 16138. [DOI](#)
  49. Sobarzo, J. C.; Pertl, F.; Balazs, D. M.; et al. Spontaneous ordering of identical materials into a triboelectric series. *Nature* **2025**, *638*, 664-9. [DOI PubMed PMC](#)
  50. Fang, Y.; Xu, J.; Xiao, X.; et al. A deep-learning-assisted on-mask sensor network for adaptive respiratory monitoring. *Adv. Mater.* **2022**, *34*, e2200252. [DOI PubMed](#)
  51. Shao, J.; Willatzen, M.; Wang, Z. L. Theoretical modeling of triboelectric nanogenerators (TENGs). *J. Appl. Phys.* **2020**, *128*, 111101. [DOI](#)

**Disclaimer/Publisher's Note:** All statements, opinions, and data contained in this publication are solely those of the individual author(s) and contributor(s) and do not necessarily reflect those of OAE and/or the editor(s). OAE and/or the editor(s) disclaim any responsibility for harm to persons or property resulting from the use of any ideas, methods, instructions, or products mentioned in the content.



© The Author(s) 2026. Open Access This article is licensed under a Creative Commons Attribution 4.0 International License (<https://creativecommons.org/licenses/by/4.0/>), which permits unrestricted use, sharing, adaptation, distribution and reproduction in any medium or format, for any purpose, even commercially, as long as you give appropriate credit to the original author(s) and the source, provide a link to the Creative Commons license, and indicate if changes were made.